

Josephson Current Induced by Ferromagnetic Resonance

We proposed the Josephson effect induced by spin waves in a Ferromagnetic Josephson junction, in which two superconductors are separated by a ferromagnetic thin layer[1]. The phenomenological model of the superconducting phase dynamics is extended to include the spin wave excitation induced by ferromagnetic resonance (FMR). The current-voltage characteristics show step structures if the microwave frequency coincides with the FMR. Our results show a new route to observe the spin wave excitation using the Josephson effect.

The Josephson effect is characterized by the zero voltage current between two superconductors (SC's) separated by a thin insulating barrier as shown in Fig. 1. This effect is a macroscopic quantum phenomenon induced by phase coherence between two superconductors. When a finite voltage-drop (V) appears in the junction, the phase difference (θ) evolves with time. As a result, an alternating current flows due to the time dependence of θ . When an alternating electric field by microwave irradiation is applied to the junction, the current-voltage (I - V) characteristics become like as a staircase, that is called Shapiro step.

The Josephson effect in the ferromagnetic Josephson junction is of considerable interest in recent years. One of the most interesting phenomena is the oscillation of the critical current with the thickness of ferromagnetic layer. The origin of oscillation is similar to that of Flude-Ferrel-Larkin-Ovchinnikov state, which is due to the exchange splitting of the conduction band in the ferromagnetic metal (FM).

Most of studies on the ferromagnetic Josephson junction have been focused on the effect of the exchange splitting on Cooper pairs penetrating into the FM. On the other hand, ferromagnetic materials possess dynamical properties such as spin wave, which is excited by using ferromagnetic resonance (FMR). Therefore, we can think that the interaction between Cooper pairs and spin waves in the FM plays an important role on the transport properties. For instance, the Andreev reflection assisted by magnons has been discussed in SC/FM junction. Up to now, however, the spin dynamics in the ferromagnetic Josephson junction has not received much attention.

We studied the effect of the spin dynamics on the Josephson effect in the ferromagnetic Josephson junction. The phenomenological model is extended to include the effect of spin wave excitations, which is a precessional motion of magnetization in the FM. As shown in Fig. 2, we found that the I - V characteristic of this model exhibits step structures and the dc Josephson current is induced by the spin wave excitation due to the FMR. In particular, the step structures appear whenever the following relation is satisfied, $2eV/\hbar = 2n\Omega$, where n is integer and Ω is the FMR frequency. We can interpret the above equation in an analogous way to the Shapiro step. In the present situation, a uniform mode of spin wave is excited in the FM by the FMR due to the microwave irradiation, and Ω correspond to the energy of quantized spin waves (magnons). If an s-wave Cooper pair penetrating into

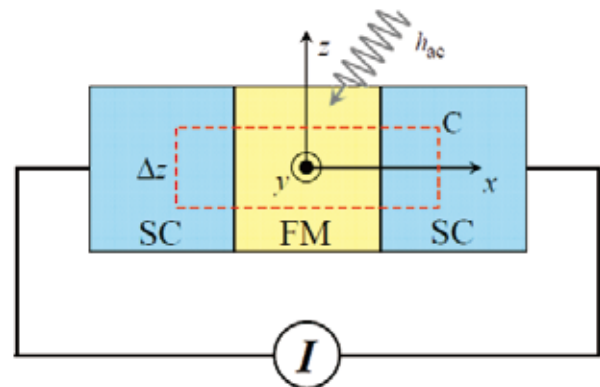


Fig. 1 A microwave radiation h_{ac} onto the ferromagnetic Josephson junction.

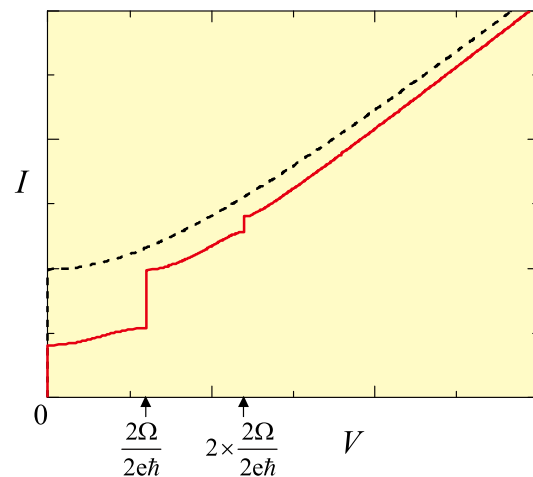


Fig. 2 Current-voltage characteristics are shown for the resonant (solid line) and non-resonant (broken line) frequencies.

the FM absorbs an odd number of magnons, the Josephson coupling vanishes between the s-wave SCs, since the formation of spin triplet state results in no Josephson coupling. On the other hand, if a number of magnons are even, the s-wave Cooper pair can go into the other superconductor. Hence, the Josephson current can flow. Our results provide a new route to observe the spin waves using the Josephson current in SC/FM/SC junctions.

References

- [1] S. Hikino, S. Takahashi, M. Mori, and S. Maekawa: J. Phys. Soc. Jpn. **77**, 053707 (2008).

Key Words

Josephson Effect, Ferromagnetic Resonance, Shapiro Step

Contact to

Sadamichi Maekawa (Theory of Solid State Physics Division)
e-mail: maekawa@imr.tohoku.ac.jp

Johansson-type Point-focusing Monochromator Crystal Realized by Hot Plastic Deformation of Ge Single-crystal Wafer

The realization of a point-focusing monochromator to increase the intensity of the X-ray beam from a conventional X-ray generator without having to broaden it at the focus has long been one of the most important aims in X-ray instrumentation. We realize such a monochromator with moderate angular resolution and high photon flux by using the hot plastic deformation of a Ge single-crystal wafer.

In 1933, Johansson proposed an advanced design of a curved crystal with its surface exactly on the focusing circle. Generally, the deformation of perfect crystals into an arbitrary shape for compact optics without deteriorating the crystal quality is not possible. Therefore, previous work has mostly concentrated either on small and precise deformation without introducing lattice defects or on large deformation with relatively broad diffraction peaks.

Recently, we developed a method of achieving the hot plastic deformation of semiconducting wafers of Si and Ge into arbitrary shapes with high accuracy [1] (see Fig.1a) without severely deteriorating the crystal quality [2]. Here, we apply this technique to realize a Johansson-type point-focusing monochromator with both large crystal deformation and high crystallographic quality. Figure 1b shows the geometric requirements for Johann- and Johansson-type monochromators. In the Johann model, X-rays diffracted from different points along the bent surface do not converge on the same point on the focusing circle. On the other hand, in the Johansson model, the lattice plane should be bent to a radius of $2R$ and the crystal surface should coincide with the focusing circle of radius R , which leads to the perfect focusing of the diffracted X-rays. As shown in Fig.1c, if the requirements are satisfied in a cylinder, the diffracted X-ray beam is focused

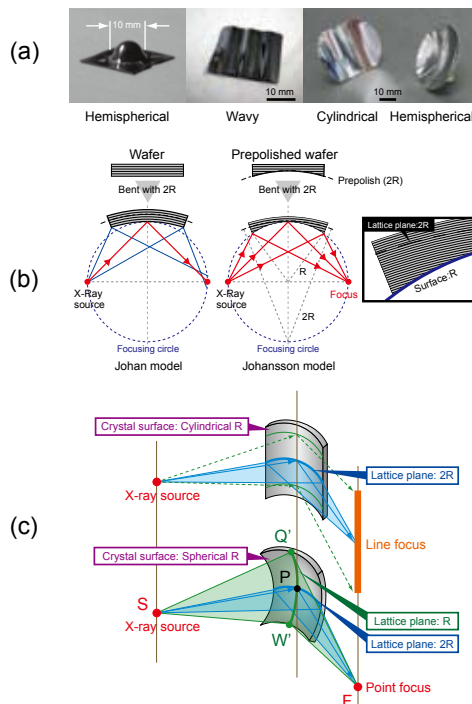


Fig. 1 (a) Si single-crystal wafers deformed by hot plastic deformation, (b) geometric requirements for Johann- and Johansson-type monochromators, and (c) schematic representation of Johansson-type line- and point-focusing geometries.

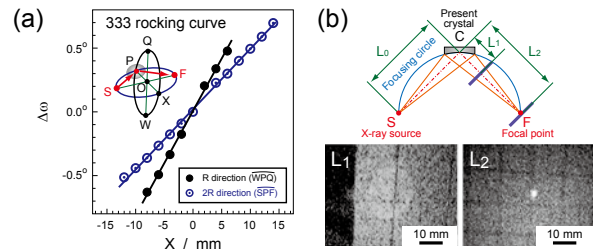


Fig. 2 (a) Curvature of the (111) plane observed by rocking-curve scans of the plastically deformed Ge (111) crystal wafer, and (b) focusing of Cu $K\alpha_1$ X-rays using the present crystal [3].

to a line. A point-focusing geometry also requires a curvature radius of R for the lattice plane in the Q'PW' direction, perpendicular to the SPF direction. Therefore, the crystal surface should be spherical with a radius of R , and the curvature radii of the lattice planes should be R and $2R$ and orthogonal to each other.

The Ge (111) wafer was polished to the shape of a cylinder with a curvature radius of 1200 mm prior to deformation to provide an appropriate offset angle between the surface and the lattice plane. It was then deformed plastically into a hemispherical shape with a radius of 600 mm at a temperature close to the melting point. The curvature of the (111) plane was evaluated by the peak shift of the 333 diffraction in an ω scan using a channel-cut incident monochromator. Figure 2a shows that the ratio of the two slopes of the peak shift agrees with Johansson's condition for lattice plane curvature. Focusing images using Cu $K\alpha_1$ radiation generated as a homogeneous divergent beam are shown in Fig. 2b. The source (S) -to-crystal (C) and crystal (C) -to-focus (F) distances were $21/2R = 850$ mm for the symmetric 333 diffraction of the crystal with $R = 600$ mm. Diffraction images were obtained 60 mm from the crystal (L_1) and 850 mm from the crystal (L_2 , at the focal point). The image at L_1 shows that the diffraction condition is satisfied simultaneously over the entire illuminated area. The pattern converges to a small circular spot of about 1.7 mm diameter at the focal point L_2 , demonstrating that a point focus is realized.

We are now attempting to fabricate this type of monochromator with much shorter radii to realize more compact systems with much higher photon flux, and we have already obtained promising results. We believe that the proposed monochromators will be of significant use to X-ray users all over the world.

References

- [1] K. Nakajima, K. Fujiwara, W. Pan and H. Okudai, Nature Materials 4, 47-49 (2005).
- [2] H. Okuda, K. Nakajima, K. Fujiwara and S. Ochiai, J. Appl. Cryst. 39, 443-445 (2006).
- [3] H. Okuda, K. Nakajima, K. Fujiwara, K. Morishita and S. Ochiai, J. Appl. Cryst. 41, 798-799 (2008).

Key Words

X-ray-point-focusing, Single-crystal, Hot-plastic-deformation

Contact to

Kazuo Nakajima (Crystal Physics Division)
e-mail: nakasisc@imr.tohoku.ac.jp

Electron Spectromicroscopy of Microstructures Capable of Six-Dimensional Characterization

The integration of electron spectroscopy into microscopy in the low energy region still remains a challenge due to the technical difficulty of achieving both high spatial and energy resolution with slow electrons. We demonstrate combined electron spectroscopy and microscopy covering the real, reciprocal and energy spaces efficiently, enabled by a low energy electron microscope (LEEM) equipped with a simple energy filter.

Combined structural analysis in real (microscopy) and reciprocal (diffraction) spaces by LEEM, also capable of real time observations, has served as a useful tool for studies of surface processes, especially for complex systems like organic materials [1]. Further integration of spectroscopy into microscopy (spectromicroscopy) will provide an even more comprehensive level of understanding of structure and property in nanoscale. Using a newly-developed energy filtering method for LEEM, efficient spectromicroscopy experiments have been carried out on Ag microstructure, where distributions of surface plasmon [2] and band structure [3] have been successfully resolved in two-dimensional (2D) real, 2D reciprocal and energy spaces.

The principle of the energy filtering, which is achieved just by adding a filter entrance slit to the LEEM, is summarized in Fig. 1. The slit position can be precisely controlled by a motor-driven micrometer and scanned across the full electron angular distribution in the backfocal plane of the objective lens. The selected electrons with different energies are dispersed by magnetic prism array to form a spectrum image at its exit. By obtaining such an E - k spectrum for each slit position, the energy and angular distribution of the incoming electrons can be measured over the full surface Brillouin zone (SBZ).

Figures 2 (a) and 2 (b) show He-I photoelectron emission micrographs (PEEM) of a complex Ag island selecting secondary electrons and d -band photoelectrons, respectively, at the conjugate backfocal plane. While the missing final states along the surface normal around the vacuum level result in darker imaging of the Ag (001) domain in Fig. 2 (a), the d -band signal is uniformly distributed over the Ag island in Fig. 2 (b). This indicates that they both reflect distribution

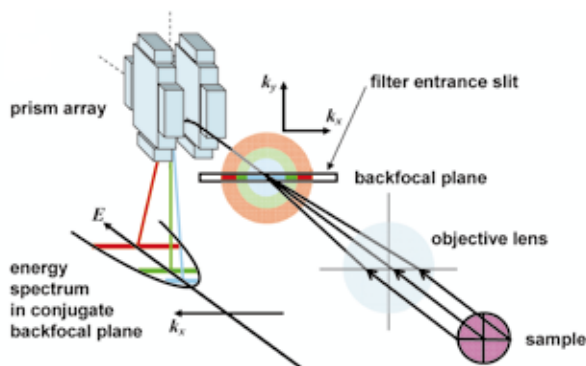


Fig. 1 Schematics of the LEEM optics equipped with a filter entrance slit in the backfocal plane. Incoming electrons with different energies (red, green and blue) have corresponding Ewald spheres (shaded disks) in the plane. The position controlled entrance slit selects a slice at a given k_y , which is dispersed by the prism array to form a parabolic energy spectrum image in the conjugate backfocal plane.

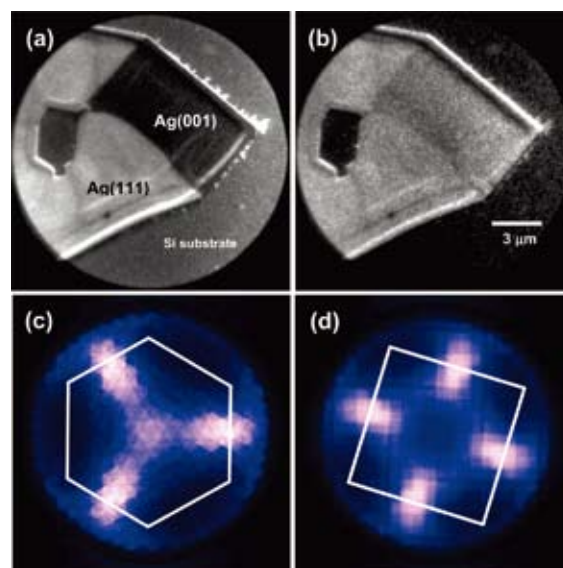


Fig. 2 Energy filtered PEEM images of a mixed Ag (111) - Ag (001) island with (a) secondary electrons and (b) d -band photoelectrons, and reconstructed energy slice images of photoelectrons at the strongest resonance distributed in the 2D reciprocal space for (c) Ag (111) and (d) Ag (001) domains. The images are symmetrised following observed symmetries by overlapping rotated images. White lines represent SBZs.

of the density of states on the Ag island, but at different energies [3]. Distribution of the electron energy loss signal from the Ag plasmon is also imaged on Ag nanoislands with spatial resolution less than 35 nm [2].

By selecting any observation area of 3.5 μm in diameter, a set of parabolic spectra covering the whole reciprocal space can be obtained. Photoelectron maps of the strongest d -band resonance are reconstructed for selected Ag (111) and Ag (001) microdomains, as shown in Figs. 2 (c) and 2 (d). They exhibit distinct 3- and 4-fold symmetries, exactly reflecting the surface symmetries of these domains [3].

The energy-filtered LEEM technique successfully visualizes electronic properties of micro- and nanostructured materials in 5D spaces. With its capability of time-resolved analysis, which adds another dimension (6D in total), it will serve as a powerful tool for structural and property control of such systems.

References

- [1] J. T. Sadowski, G. Sazaki, S. Nishikata, A. Al-Mahboob, Y. Fujikawa, K. Nakajima, R. M. Tromp and T. Sakurai, Phys. Rev. Lett. **98**, 046104 (2007).
- [2] Y. Fujikawa, T. Sakurai and R. M. Tromp, Phys. Rev. Lett. **100**, 126803 (2008).
- [3] Y. Fujikawa, T. Sakurai and R. M. Tromp, Phys. Rev. **B79**, 121401 (R) (2009). (Editors' Suggestion)

Key Words

LEEM, PEEM, Spectromicroscopy

Contact to

Yasunori Fujikawa (Surface and Interface Research Division)
e-mail: fujika-0@imr.tohoku.ac.jp

Optical Properties of Dislocations in Wurtzite ZnO Bulk Single-Crystals Introduced at Elevated Temperatures

Defects inducing long-range strain fields, as dislocations, are of considerable importance in semiconductor electronics, since they affect the electronic properties of semiconductor devices. Recently, ZnO is expected for UV light-emitting devices and is supposed that dislocations are more easily introduced than GaN. However, the optical properties of dislocations in ZnO have not been fully elucidated.

Despite considerable success in optimizing the growth conditions and structural quality, ZnO epitaxial layers still contain a high density of defects that influence their optoelectronic properties. Most characteristic defects, investigated by transmission electron microscopy (TEM), are high-density (typically 10^9 - 10^{11} cm⁻²) dislocations passing through entire layers. In ZnO, dislocations are introduced with lower stress and are much mobile, in comparison with in GaN [1]. Since dislocations can influence the device performance through non-radiative recombination, etc., the knowledge of the influence of dislocations is required for the practical use of this material. Even though ZnO has the same crystal structure as GaN, however, the influence of dislocations in ZnO has not been fully elucidated. We have examined the optical properties of dislocations in ZnO bulk single-crystals in which an arbitrary number of dislocations were newly introduced by plastic deformation, at temperatures comparable to the typical temperatures for the fabrication of ZnO-based devices, by photoluminescence (PL) spectroscopy and TEM [2, 3].

Wurtzite ZnO bulk single-crystals were compressively deformed at elevated temperatures 923 - 1123 K to introduce an arbitrary number (10^9 - 10^{10} cm⁻²) of fresh dislocations with the Burgers vector of $a/3\langle 1120 \rangle$ (the inset in Fig. 1 (a)). Deformed specimens showed excitonic PL light emission with photon energies of 3.100 and 3.345 eV, as well as their LO phonon replicas (with the separation between the nearest-neighbor emission lines of 72 meV) at 11 K (Figs. 1 (a) and (b)). The PL intensity for the 3.100 and 3.345 eV emission bands increased monotonously with increasing deformation temperature (Fig. 1 (c)). Those emission bands were, therefore, formed as a result of the introduction of dislocations at the elevated temperatures. On the other hand, the introduction of the dislocations did not influence the intensities of the other emission bands such as the free-excitonic (FX) emission band (Figs. 1 (a) and (c)). This characteristic of ZnO may be an advantage over GaN, since GaN exhibits a phenomenon that all intensities decrease with introduction of dislocations [4].

The PL intensity for the 3.100 and 3.345 eV emission bands decreased via two thermal quenching processes (Fig. 2). It was shown that, the quenching process arose at lower temperatures (at around 30 K) was due to the transition from an excitonic recombination at a localized level to a recombination between the level and a band (a bound-to-free transition), and that arose at higher temperatures was due to a thermal escape of carriers from the localized level to a band. The activation energy for the latter quenching process of the 3.100 eV emission band ($\Delta E_{3.100}$) or that of the 3.345 eV emission band ($\Delta E_{3.345}$), which corresponded to the depth of the localized energy level associated with the 3.100 or 3.345 eV emission band, was estimated to be 0.3 or 0.05 eV, respectively. Actually, the difference of the 0-phonon peak energies for the FX emission band and the 3.100 eV one corresponded to $\Delta E_{3.100}$; i.e., $3.378 \text{ eV} - 3.100 \text{ eV} = 0.278 \text{ eV}$ at $T = 11 \text{ K}$. Also, the difference for the FX emission band and the 3.345 eV one was close to $\Delta E_{3.345}$; $3.378 \text{ eV} - 3.345 \text{ eV} = 0.033 \text{ eV}$ at 11 K.

The Huang-Rhys factor for the 3.100 eV emission band and that for the 3.345 eV one were, respectively, estimated to be 1.4 and 0.2. They differed from the factors for the other emission bands, including the factor for the 3.2108 eV emission band (~0.5) induced by

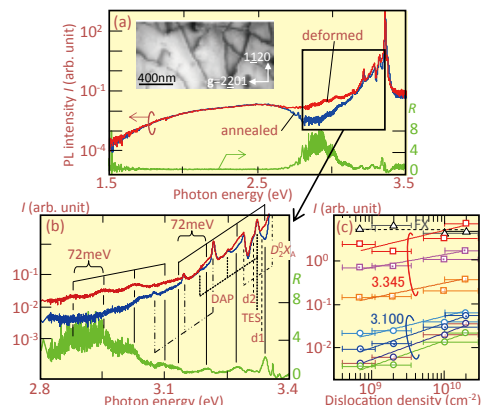


Fig. 1 The logarithmic PL intensity versus the photon energy for a specimen; deformed at 923 K (the red curve) or annealed at 923 K without stress (the blue curve). The ratio of those PL intensities, $R = I_{\text{deformed}}/I_{\text{undeformed}}$, is also shown (the green curve). A part of (a) is magnified in (b). The inset in (a) shows a TEM image of dislocations in the deformed specimen. (c) The PL intensity at the peak energy of an LO phonon line as a function of dislocation density. The open marks, the marks with dot, those with "+", and those with "-" show the data for the 0-, 1-, 2-, and 3-LO phonon lines, respectively.

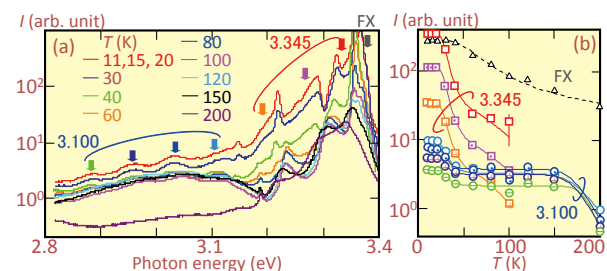


Fig. 2 (a) PL spectra for a deformed specimen (the deformed temperature; 923 K) obtained at various temperatures T . (b) T -dependence of the peak intensity of an LO phonon line. The meaning of the marks is the same as in Fig. 1 (c)

deformation at room temperature but were not induced at elevated temperatures. Also, no obvious polarization was observed for the emission bands. From those results, it was suggested that point defect complexes involving dislocations are the candidates for the origin of the localized energy levels associated with the emission bands.

References

- [1] I. Yonenaga, H. Koizumi, Y. Ohno, and T. Taishi, *J. Appl. Phys.* **103**, 093502 (2008).
- [2] Y. Ohno, H. Koizumi, T. Taishi, I. Yonenaga, K. Fujii, H. Goto, and T. Yao, *Appl. Phys. Lett.* **92**, 011922 (2008).
- [3] Y. Ohno, H. Koizumi, T. Taishi, I. Yonenaga, K. Fujii, H. Goto, and T. Yao, *J. Appl. Phys.* **104**, 073515 (2008).
- [4] I. Yonenaga, H. Makino, S. Itoh, T. Goto, and T. Yao, *J. Electron. Mater.* **35**, 717 (2006).

Key Words

Dislocations, ZnO, Electronic Structures

Contact to

Yutaka Ohno (Physics of Crystal Defects Division)
e-mail: yutakaohno@imr.tohoku.ac.jp

Nano Precipitation in Fe-C-M Martensitic Steels During Nitriding

Nitriding is one of the most important surface treatments used in industry to increase surface hardness and improve the fatigue strength. Compared with other surface hardening treatments accompanying quenching (carburizing, induction heating and so on), this process, which utilizes precipitation hardening by fine alloy nitrides, has several advantages as listed in the following;

- (1) Smaller strain accompanying heat treatment
- (2) Higher hardness achievable
- (3) Excellent heat resistance

and thus, attracts more attention recently in needs of much higher precision in size scale of structural parts after heat treatment.

Here we report our recent study on nano-sized precipitation of alloy nitrides in Fe-C-M (M: substitutional alloying element) martensitic steels during plasma nitriding [1]

Fig. 1 shows hardness profiles of Fe-0.6C, Fe-0.6C-1Al and Fe-0.6C-1Cr alloys nitrided at 823K for 57.6ks. In the plain carbon steel, surface hardness hardly changes during nitriding but largely increases in the alloyed steels. It reaches 650HV in the Fe-0.6C-1Al alloy and 550HV in the Fe-0.6C-1Cr alloy

Fig. 2 (a) shows SEM micrographs of the nitrided layer (depth ~ 200 μ m) in Fe-0.6C-1Cr alloy. Cementite precipitates at various boundaries in lath martensite structure (lath, block and packet boundaries and prior austenite grain boundaries) in the nitrided layer as well as in the unnitrided region. The size of cementite is finer in the alloyed steels. In the nitrided layer of Fe-C alloy, plate-shape iron nitrides (Fe₄N or Fe₁₆N₂) are formed during furnace cooling in addition to cementite. In the Fe-0.6C-1Al and Fe-0.6C-1Cr alloys, much finer alloy nitrides are formed by nitriding

Fig. 2 (b) shows the bright field image and the corresponding selected area diffraction pattern of the surface region (~40 μ m) of the Fe-0.6C-1Cr alloy nitrided at 823K for 57.6ks. Much finer plate-shape precipitates lying on {100} planes of the matrix are formed uniformly. Their length and thickness are about 20nm and several atomic layers, respectively. High resolution electron microscopy clarified that those are B1-type CrN. In the Fe-0.6C-1Al alloy, on the other hand, platelet AlN of which length and thickness are about 100nm and a few nm, respectively, is lying on {100} planes of the matrix in martensite laths (Fig. 2 (c)). Both of them have a Baker-Nutting orientation relationship ([001] α //[001]_{MN}, (100) α //(110)_{MN}) with respect to the ferrite matrix. These

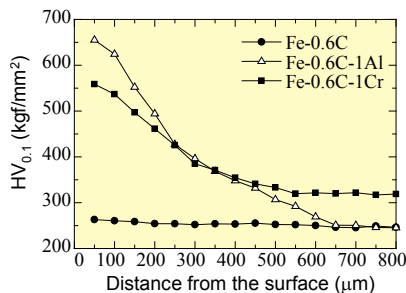


Fig. 1 Hardness profiles of Fe-0.6C, Fe-0.6C-1Al and Fe-0.6C-1Cr alloys nitrided at 823K for 57.6ks.

Alloy	Increase of surface hardness Δ HV
Fe-1Al (ferrite)	10
Fe-0.6C-1Al (martensite)	400
Fe-1Cr (ferrite)	520
Fe-0.6C-1Cr (martensite)	250

Table. 1 Increase of surface hardness in Fe-M ferritic alloys and Fe-C-M martensitic alloys (nitrided at 823K for 57.6ks).

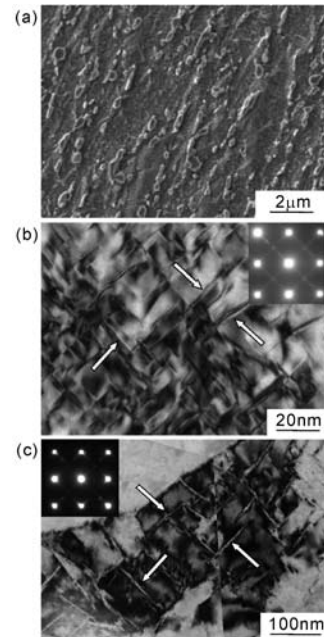


Fig. 2 (a) SEM micrograph of Fe-0.6C-1Cr nitrided at 823K for 57.6ks. (b) TEM bright field image and corresponding selected area diffraction pattern of the surface region (depth~40 μ m) of (b) Fe-0.6C-1Cr and (c) Fe-0.6C-1Al nitrided at 823K for 57.6ks. Incident beam is parallel to [001] α

precipitates are the same as reported in nitrided Fe-M binary alloys [2]. From these results, increases in hardness in Fe-0.6C-1Al and Fe-0.6C-1Cr alloys are attributed to precipitation of plate-shape AlN and plate-shape CrN, respectively.

Increases of surface hardness in martensite and ferrite nitrided for 57.6ks are compared in Table 2. In Al-added alloys, hardness increase in martensite is larger than in ferrite. Since AlN nucleates at dislocations, it is concluded that high density of dislocations in lath martensite promotes the precipitation of AlN. On the other hand, in Cr-added alloys hardness increase in martensite is smaller than in ferrite. This is attributed to decrease in volume fraction of fine CrN precipitated in the lath. As-quenched martensite is tempered during heating before CrN precipitation starts. In this period, Cr is enriched into the cementite whereas Cr concentration in the matrix decreases. Since the Cr-rich cementite is converted to coarse massive CrN during prolonged nitriding, precipitation of fine plate-shape CrN within the lath might decrease. This results in lower surface hardness in martensite than in ferrite of the Cr-added alloys.

References

- [1] Y. Tomio, S. Kitsuya, G. Miyamoto and T. Furuahara: Proc. the 17th International Federation for Heat Treatment and Surface Engineering (IFHTSE) Congress, 2009, in press.
- [2] Y. Tomio, G. Miyamoto, T. Furuahara and T. Maki: Proc. the 3rd Int. Conf. on Advanced Structural Steels (2006) 460-464.

Key Words

Steel, Precipitation, Surface Heat Treatment

Contact to

Tadashi Furuahara (Microstructure Design of Structural Metallic Materials Division)
e-mail: furuhara@imr.tohoku.ac.jp

Paving the Way to High-Quality Indium Nitride -The Effects of Reactor Geometry and Pressure-

Indium nitride (InN), with band gap energy of about 0.7 eV, is a promising material for fabricating devices such as laser diodes for high-performance optical communications systems and field effect transistors. However, it is very difficult to grow InN due to the extremely high solid-vapor phase equilibrium pressure of nitrogen. Here, we design some new reactors to meet this challenge and confirm those effects in InN growth.

Most of the industrial semiconductor devices have been grown by metalorganic vapor phase epitaxy (MOVPE) since it provides large scale productions, precise composition controls, and flexible layer designs by supplying variable MO sources. The geometry of MOVPE reactors includes vertical and horizontal types. The reactor pressure generally covers from low pressure (LP) to atmospheric pressure (AP). The LP MOVPE reactors are widely adopted for reducing the thermal convection effect, and have led to the great commercial successes in InGaAsP to InGaAlP-based devices. However, the growth of the attractive InN film is still a tough challenge for the LP and AP MOVPE due to the extremely high solid-vapor phase equilibrium pressure of nitrogen, which limits the growth temperature approximately below 600°C, hindering the growth of high-quality InN. With further increasing the growth temperature, the surface morphology will deteriorate and sponge-like structures are inclined to appear. In addition, our vertical reactor provides too small InN growth rate of about 20 nm/h for device applications.

In order to increase the growth rate, we modified the vertical reactor (Fig. 1 (a)) into a horizontal one (Fig. 1 (b)) with a narrow flow channel [1]. As a result, the growth rate of the InN films in the horizontal reactor significantly increases 10 to 20 times larger than that in the vertical reactor at 550~575°C. This is due to the reduction of the stagnant layer thickness, the increases in the source supply to the substrate surface and the high concentration of the source gases by narrowing the flow channel.

Here, it should be noted that the above reactors work from LP to AP. Although the growth rate increases for the horizontal reactor, the problem of the sponge-like films still

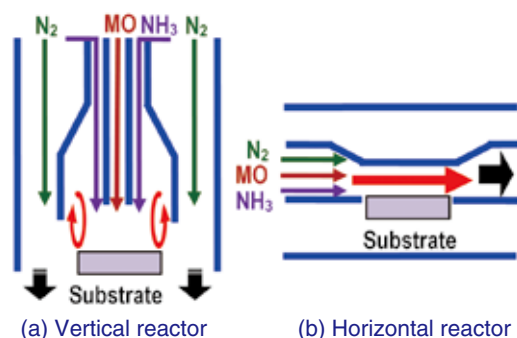
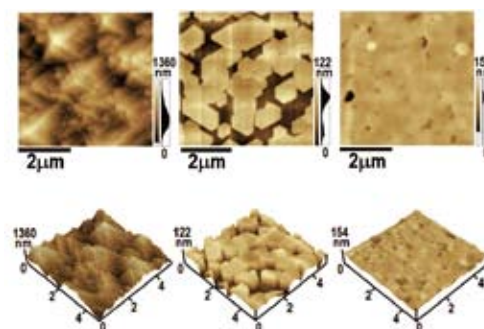


Fig. 1 Schematic diagrams of the reactor geometry. Thermal convection easily occurs for the vertical reactor with a large diameter flow channel (a), but relieved for the horizontal reactor with a very narrow flow channel (b). For InN growth, trimethylindium was used as a group-III MO source, NH₃ as a group-V source, and N₂ as a carrier gas. The growth pressure was 650 Torr.



(a) 650 Torr (b) 1200 Torr (c) 1600 Torr

Fig. 2 Atomic force microscope images of the InN films grown at 675°C under 650 Torr with pyramidal structures (a), 1200 Torr with hexagonal platelet structures (b), and 1600 Torr with a well-coalesced surface (c). Note that all the InN films were directly grown on sapphire substrates, which were just pretreated in NH₃ ambient at high temperature.

exists for the higher temperature growth (>600°C). Therefore, we designed a pressurized reactor (PR) which can work above the AP, so as to increase the nitrogen pressure and enhance the lateral growth of the InN films.

The surface morphology of the InN films is shown in Fig. 2, where pyramid-like, platelet-like, and well-coalesced structures can be observed for the InN grown under 650, 1200, and 1600 Torr, respectively. It is indicating that the InN surface tends to be flat under higher reactor pressures, which favors the growth of the low-index plane of crystals, such as (0001) plane parallel to the substrate surface [2]. This case is similar to gallium nitride, where pyramid-like structure and platelet-like structure correspond to the growth under 76 and 760 Torr, respectively [3].

The above results shed a new light on MOVPE growth of InN, which has been suffering from the various difficulties during the last decade. By stabilizing the (0001) plane growth, PR-MOVPE is promising for the growth of high-quality dense InN films at higher growth temperature, making a step closer to the InN applications in the optoelectronic devices.

References

- [1] Y. H. Liu, T. Kimura, T. Shimada, M. Hirata, M. Wakaba, M. Nakao, S. Y. Ji, and T. Matsuoka, *phys. stat. sol. (c)*, **6**, S381 (2009).
- [2] Y. H. Liu, Y. T. Zhang, T. Kimura, M. Hirata, Y. Ohta, S. Y. Ji, and T. Matsuoka, *The 56th Spring Meeting of Jpn. Soc. Appl. Phys. and Rel. Soc.*, Tsukuba Univ., Mar. 31, 2009.
- [3] T. Sasaki and T. Matsuoka, *J. Appl. Phys.* **77**, 192 (1995).

Key Words

InN, MOVPE, PR-MOVPE Growth

Contact to

Takashi Matsuoka (Physics of Electronic Materials Division)
e-mail: matsuoka@imr.tohoku.ac.jp

Structure of Liquid LiNbO₃ analyzed by Energy Dispersive X-ray Diffraction

The structural analysis of the liquid LiNbO₃ at 1550K has been carried out by the energy dispersive X-ray diffraction (EDXD). The distorted NbO₆ units with a disparity in the first Nb-O atomic pairs were well confirmed as the fundamental local structural unit in liquid LiNbO₃.

In order to improve the single crystal quality produced by the ordinary Czochralski method, a variety of physic-chemical properties of liquid LiNbO₃ have been measured. The variations in such physical properties indicate an anomalous behavior just above its melting point (1526K) and the structure analysis of liquid LiNbO₃ near the melting point is strongly required so as to elucidate the structural origin of such anomaly. Although the ordinary angular dispersive X-ray diffraction technique by using Mo K α radiation (ADX) allows us to obtain structural information for this purpose, the obtained structural factor less than about 150nm⁻¹, produces a serious limitation to make the interesting discussion on the local ordering structure. The energy dispersive X-ray diffraction (EDXD) is known to be one of the most useful experimental methods, which serve the structural information in the large wave vector region over 200nm⁻¹ [1]. This strongly prompted us to apply this advanced EDXD technique to the structural analysis of liquid LiNbO₃ [2].

The resultant $Q(S(Q)-1)$ and corresponding RDF are given in Fig.1 and Fig.2, respectively. The present EDXD-RDF data is superior to that of the conventional ADXD-RDF [3] in its resolution because the upper limit of Fourier transformation is increased up to 230 nm⁻¹. In particular, a hump at larger r side of the first Nb-O correlation peak at about 0.190nm is clearly observed in the EDXD-RDF, which indicates an appreciated disparity in the nearest-neighbor Nb-O atomic pairs. Such geometrical features in the local ordering units of oxide compounds are frequently realized in coordination polyhedra linked by sharing their edges or faces. Therefore, rather distorted NbO₆ octahedron and its linkage can be suggested as one of the common local structural image in liquid LiNbO₃. Although there is a close correspondence in the correlation distances of the liquid and crystalline LiNbO₃ up to about 0.4 nm, the RDF of liquid LiNbO₃ indicates a relatively lower probability of finding correlations at around 0.4 nm than that expected from the first Nb-Nb (0.383 nm) and Nb-O (0.388 nm) pairs in the crystalline structure. Since this range of distances corresponds to the distribution of NbO₆ octahedra in the crystalline structure, the structure of liquid LiNbO₃ can be featured by its unique distribution of NbO₆ octahedra.

In order to discuss the detailed structure of liquid LiNbO₃, we employed the reverse Monte Carlo (RMC) simulation technique where the atomic configurations are estimated rather simply on the grounds of their consistency with the experimental data [4]. The present RMC simulation results are found to reproduce the independent interference functions $Q(S(Q)-1)$ well, as shown in Fig.1. The obtained partial structure factors indicate that the correlations of $a_{NbNb}(Q)$ agrees well with the position of the shoulder at about $Q=21\text{nm}^{-1}$ enhanced near the melting point of LiNbO₃ [3]. This feature, in particular, is quite likely to correlate with the shoulder attributed to the development of clusters originated from a clear Nb-Nb

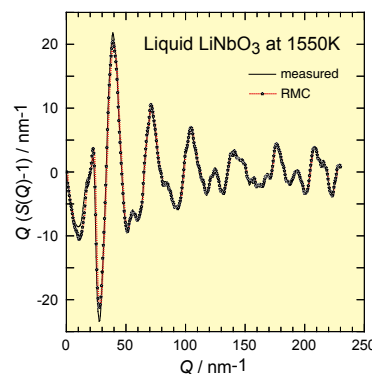


Fig. 1 $Q(S(Q)-1)$ of liquid LiNbO₃. The solid line is the EDXD result, and dotted line is the RMC simulation.

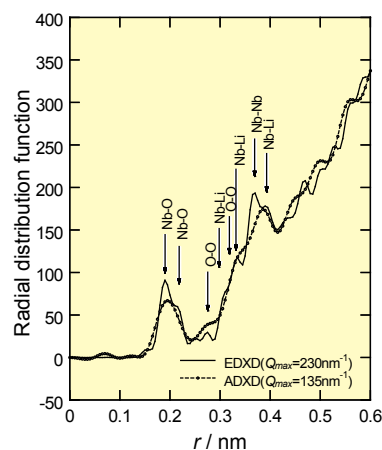


Fig. 2 The solid line is the EDXD-RDF, and dotted line is the ADXD-RDF [2]. The arrows indicate atomic pairs in the crystalline LiNbO₃.

correlation. The development of Nb-Nb correlation may be one of the important reasons for the origin of anomalous behavior detected in the physical properties in the liquid state near the melting point. It would be of great interest to apply the present analytical approach to the structural investigation of high temperature liquids near melting points.

References

- [1] K.Sugiyama, V.Petkov, S.Takeda, Y.Waseda, Sci. Rep. Res. Inst. Tohoku Univ. **A38** 1 (1993).
- [2] K.Sugiyama, M.Saito, Y.Waseda, J. Crystal Growth. **311** 966 (2009).
- [3] K.Sugiyama, K.Nomura, Y.Waseda, P.Andonov, S.Kimura, K.Shigematsu, Z. Naturforsch. **45a** 1325 (1990).
- [4] M.Saito, C.Park, K.Omote, K.Sugiyama, Y.Waseda, J. Phys. Soc. Japan, **66** 633 (1997).

Key Words

Liquid Structure, X-ray Diffraction, EDXD

Contact to

Kazumasa Sugiyama (Non-Crystalline Materials Division)
e-mail: kazumasa@imr.tohoku.ac.jp

Mechanically and Biologically Biocompatible Metallic Material Fabricated by Combining Porous Titanium with Medical Polymer

One of the concepts for preparing novel metallic biomaterials possessing both an ultra-low Young's modulus that is almost the same as that of human bone and biofunctions usually possessed by living tissues is proposed in the present study. By introducing pores in bulk materials, the Young's modulus of the materials can be reduced to almost the same value as that of bone. Further, filling pores of porous materials with a polymer possessing a certain biofunction is expected to cause the biofunctionalization of the porous materials. Therefore, porous titanium (pTi) filled with polymethylmethacrylate (PMMA) was fabricated using a new process developed in our laboratory. Then, the effect of the PMMA filling on the tensile strength and Young's modulus of pTi was examined. As a result, it was found that the PMMA filling was useful for improving the tensile strength while maintaining a low Young's modulus of pTi.

A low Young's modulus similar to that of bone is one of the important properties of metallic biomaterials, because it is advantageous to inhibit bone atrophy and absorption due to stress shielding. It is considered that the use of porous materials is one of the most effective techniques for achieving a low Young's modulus. However, the mechanical properties of porous materials deteriorate with an increase in porosity. This deterioration may be attributable to stress concentration near the pores of porous materials. Thus, the stress concentration can be reduced by filling the pores with certain materials, which in turn is expected to improve the mechanical properties of the porous materials. In such a case, materials having a low Young's modulus should be selected for filling, in order to prevent an increase in the Young's modulus. Furthermore, depending on the type of filled materials, biofunctions, which are not intrinsically present in metallic materials, can be introduced to the porous materials, in addition to the improvement in mechanical properties. In this study, pores of pTi were filled with a medical polymer, PMMA, and then, the effects of the PMMA filling on the mechanical properties of pTi were investigated as a model case [1].

In order to prepare pTi, pure titanium powders were sintered at a constant temperature. Some pTi specimens having porosities in the range of 22–50% were obtained as shown in Fig. 1. The pTi specimens are labeled according to the maximum particle diameter of pure titanium powders and the porosity of pTi. Some tensile specimens of pTi were subjected to silane coupling treatment (Si treatment) before carrying out PMMA filling. A tensile specimen of pTi was

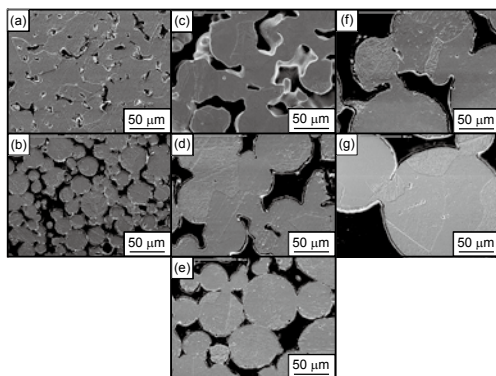


Fig. 1 SEM micrographs of cross sections of (a) pTi45-22, (b) pTi45-35, (c) pTi150-27, (d) pTi150-38, (e) pTi150-45, (f) pTi250-45, and (g) pTi250-50.

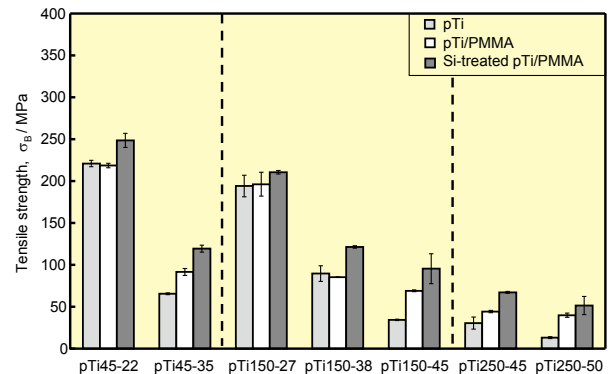


Fig. 2 Tensile strengths of pTi, pTi/PMMA, and Si-treated pTi/PMMA.

soaked in a monomer solution mixed with a polymerization initiator. After removing air bubbles in pores under reduced pressure, the infiltrated monomer solution was polymerized by heating it at a constant temperature under atmospheric pressure. Then, the unwanted part of PMMA was removed by mechanical machining.

Figure 2 shows the tensile strengths of pTi, pTi filled with PMMA (pTi/PMMA), and Si-treated pTi/PMMA; they decrease with an increase in porosity. However, in the high porosity range, the tensile strengths of pTi/PMMA are higher than those of pTi. This result indicates that the effect of the PMMA filling on the improvement in the tensile strength of pTi is limited to the low tensile strength range. In contrast, in the case of Si-treated pTi/PMMA, even higher tensile strength is obtained, and this improvement is not limited by porosity. Further, Young's moduli of pTi, pTi/PMMA, and Si-treated pTi/PMMA were measured using the stress–strain curve obtained by the tensile test. It was observed that the PMMA filling had a very small influence on the Young's modulus of pTi, because the Young's modulus of PMMA is lower than that of pTi.

The developed process of filling the pores of porous materials with a polymer is expected to be applicable also to polymers other than PMMA. By selecting an appropriate polymer, biofunctions can be added to porous materials. For example, if pores are filled with a biodegradable polymer mixed with an agent for promoting bone formation and growth, osteoconductivity is expected to improve and be higher than that in the case of pTi with unfilled pores. On the basis of this concept, we have initiated the application of the developed process to poly-L-lactic acid (PLLA), which is one of the practical biodegradable polymers for biomedical applications, as a next step in this study.

References

[1] M. Nakai, M. Niinomi, T. Akahori, H. Yamanoi, S. Itsuno, N. Haraguchi, Y. Itoh, T. Ogasawara, T. Onishi and T. Shindoh, *Japan Inst. Metals*, 72 (2008) 839–845.

Key Words

Biomaterial, Porous Material, Metal/Polymer Composite

Contact to

Mitsuo Niinomi (Biomaterials Science Division)

e-mail: niinomi@imr.tohoku.ac.jp

Highly-Glass Formable and Biocompatible Ti-based Metallic Glasses

Ti-based metallic glasses have a great potential as structural materials due to their good mechanical properties, chemical properties and excellent processing performance owing to unique thermal properties [1, 2]. Meanwhile, pure titanium and some of its alloys show good performances for biomaterials according to their mechanical and chemical properties [3].

We designed our new system of Ti-based metallic glasses by investigating restricted alloying elements biocompatible for dental implants and selected high glass formable Ti-based metallic glasses. The Ti-based metallic glasses do not contain Al, V and Ni elements which are well known to be neurotoxicity and cytotoxicity for human body. Current medical reports of impracticability by these elements have been a hot issue in biomaterials science. Our newly designed Ti-Zr-Pd-Cu-Sn-P metallic glasses, namely the $Ti_{45}Zr_{10}Pd_{10}Cu_{35-x}(Sn_{0.83}P_{0.17})_x$ ($x=3, 5$ and 6) alloys, have a high potential to be applied for biomaterials as dental implant. The detailed results are summarized as follows:

$Ti_{45}Zr_{10}Pd_{10}Cu_{35-x}(Sn_{0.83}P_{0.17})_x$ ($x=3, 5$ and 6) metallic glasses were fabricated by mold casting technique. $Ti_{45}Zr_{10}Pd_{10}Cu_{35-x}(Sn_{0.83}P_{0.17})_x$ ($x=3, 5$ and 6) metallic glasses exhibits wide supercooled liquid regions ($\Delta T_x = T_x - T_g$) $> 60K$, high reduced glass transition temperatures ($T_{rg} = T_g/T_l$) > 0.59 and γ parameters ($T_x / (T_g + T_l)$) ≥ 0.40 . Here, T_x , T_g and T_l are crystallization, glass transition and liquidus temperatures, respectively. Its critical rod diameter for fully amorphous sample is 5 mm (Figure 1).

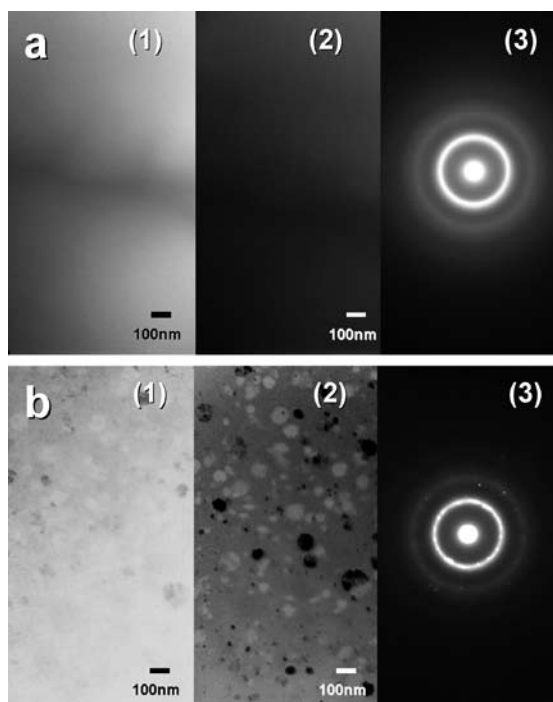


Fig. 1 The structure of the $Ti_{45}Zr_{10}Pd_{10}Cu_{30}Sn_{4.15}P_{0.85}$ bulk glass rod samples of 5.0mm (a) and 5.5mm (b) in diameter in as-cast state, TEM. (1) – Bright-field image, (2) – dark-field image and (3) – selected-area electron diffraction (SAED) patterns

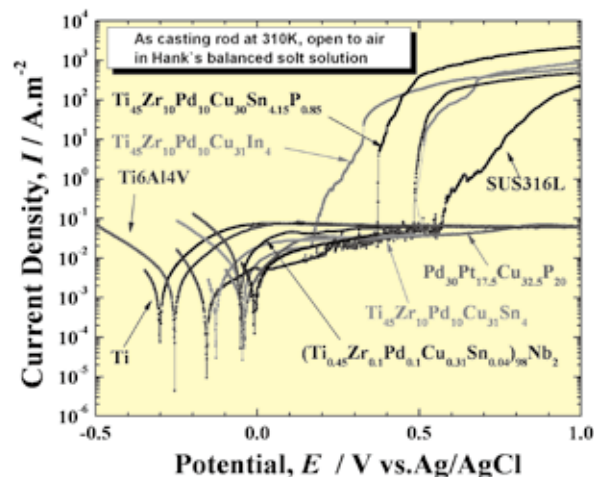


Fig. 2 Anodic polarization curves in HBSS aqueous solutions open to air at 310 K (the exposed area was 1 cm^2)

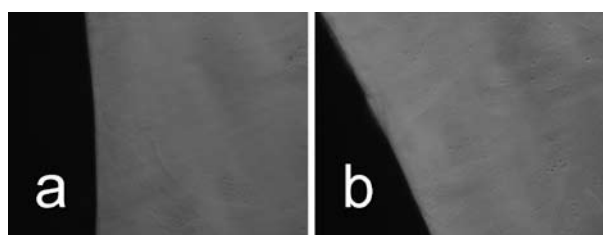


Fig. 3 Evaluation of cytotoxicity for as-cast $Ti_{45}Zr_{10}Pd_{10}Cu_{32}Sn_{2.49}P_{0.51}$ (a) and $Ti_{45}Zr_{10}Pd_{10}Cu_{29}Sn_{4.98}P_{1.02}$ (b) metallic glass cylindrical rods with a diameter of 3.5mm in osteoblasts at 310 K for 7 days

Especially, the optimized Ti-based metallic glass has high corrosion resistance with better passivity in a wide passivation range in simulated body fluids at 310K (Figure 2). In addition, biocompatibility of Ti-based metallic glasses was also evaluated by cell culture in vitro. Excellent biocompatibility of these Ti-based metallic glass shows high potentials to be applied as biomaterials that necrosis of osteoblast (SaOS2) was not detected in this study (Figure 3).

References

- [1] A. Inoue: *Acta Mater.*, **48** (2000), p.279
- [2] J. -J Oak, D. V. Louzguine, A. Inoue: *J. Mater. Res.*, **22** (2007), p.1346
- [3] S. Steinemann. *Ti '84 Science and Technology*, G. Lütjering, U. Zwicker and W. Bunk, Eds. (1984) p.1373.

Key Words

Metallic Glass, Biocompatibility, Dental Implant

Contact to

Hidemi Kato (Laboratory of Non-equilibrium Materials Division)

e-mail: hikato@imr.tohoku.ac.jp

How to Push the Stubborn Protein to Appear on the Growth Scene

We can handle the nucleation of white hen-egg lysozyme crystal in either way of enhancement or retard via applying an external electric field. This is attributed to the manipulation of the magnitude relation of an electrical permittivity of lysozyme between crystal and solution by varying frequency of the applied field.

Nucleation of protein crystals is never easy going. We need to wait a week, a month or more with patience to see their appearance in a small solution cell. This is because they have a fairly complex structure with high molecule weights. The enigmatic behavior of water complex surrounding the fragile protein makes its birth more difficult. Tons of refined researches have been tried to stimulate the silent solution to initiate the nucleation, i.e., stirring the solution, radiating laser or ultrasonic sound on the solution, etc. Some worked and some did not. However, such techniques can change the nucleation in only one way, i.e., enhancement or retard. And the worse thing is that the retardation is most often observed.

Applying an external electric field, proposed here, may be a unique solution to this problem. The solution principle is simple. Nucleation occurs due to the difference in chemical potential between solid and solution. This means if we can manage the energy difference in some way, we can control

the nucleation. An external electric field adds an electrostatic potential to the chemical potential of both solid and liquid and would change the energetic relationship between them. The new thermodynamic state brings about a change in driving force for nucleation. We have demonstrated the retard of the nucleation rate of YBCO by the imposition of an electric field as large as 10^4 V/cm that is sustained in the electric double layer between the solid and liquid [1]. However, it is not possible to enhance the nucleation of YBCO since the magnitude relation of an electrostatic potential between solid and liquid cannot be reversed with an electric field that is practically applied.

Because the electrostatic potential added to chemical potential is a function of an electrical permittivity, ϵ , and an applied electric field, E , i.e., $\partial\epsilon/\partial x E^2$ (x denotes composition), its magnitude relation between solid and liquid could be reversed if an electrical permittivity would change. This is possible for organic materials such as lysozyme due to the dispersion of their electrical permittivity in the range of 0 ~ 1 MHz with several hundred applied voltage. In contrast inorganic material requires GHz-order frequency for the conversion that is not practically possible.

Nucleation in a small droplet of lysozyme solution under an electric field with different frequency was investigated (Fig. 1). It is interesting to see that the nucleation of lysozyme can be either enhanced or retarded by choosing appropriate frequency of an applied electric field (Fig. 2). This is the first work that demonstrates the control of nucleation of lysozyme in either way of enhancement or retard by an applying electric field [2].

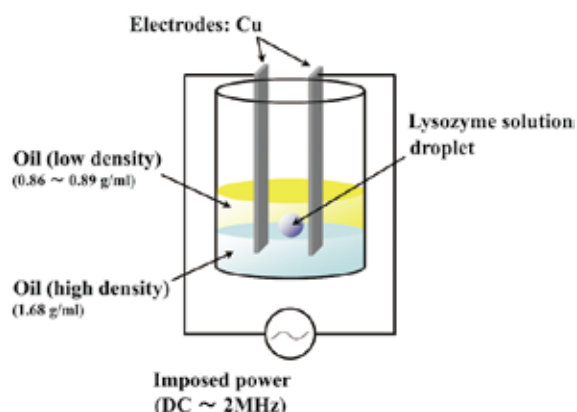


Fig. 1 Experimental set up for the nucleation in a droplet of lysozyme solution encapsulated in oil. An externally applied electric field of 860 V/cm brings about an effective electric field as large as $\sim 10^5$ V/cm in an electric double layer which forms at the solid-liquid interface.

References

- [1] X. Huang, S. Uda and S. Koh, *J. Cryst. Growth*, **307**, 432 (2007).
- [2] H. Koizumi, K. Fujiwara and S. Uda, *Crystal Growth & Design*, **9**, 2420 (2009).

Key Words

Electric Field, Nucleation, Lysozyme

Contact to

Satoshi Uda (Crystal Chemistry Division)
e-mail: uda@imr.tohoku.ac.jp

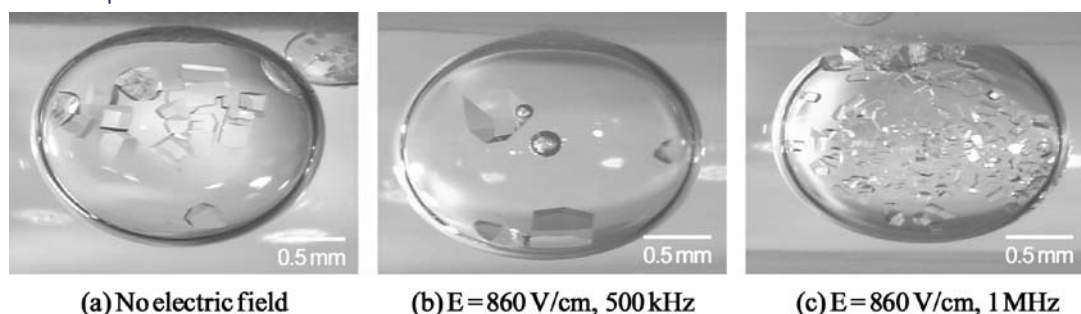


Fig. 2 Number of lysozyme crystals appearing in a droplet depends on the frequency of an applied electric field. They reflect the frequency-dependent nucleation rate.

High-speed and Low Temperature Coating of α -Al₂O₃ on Cutting Tools by Laser CVD

α -Al₂O₃ coating is essential for cutting tools to improve performance and to elongate the lifetime. The low-temperature deposition of α -Al₂O₃ films enables one to expand wide applications of Ti (C, N) -based cermet cutting tools. Laser chemical vapor deposition (LCVD) can coat α -Al₂O₃ films directly on Ti (C, N) materials at low temperature and high deposition rate, which has never been attained by conventional coating techniques.

Tungsten (W) is an indispensable resource for cutting tools because of the wide usage for WC-Co cemented carbides. However, W is a localized element on earth, and then the substitution of W for other elements is a recent key technology for cutting tool industry. Ti (C, N) -Ni cermets can be a promising candidate due to abundance of Ti element and high hardness. The cutting performance of WC-Co cemented carbide and Ti (C, N) -Ni cermets strongly depends on the surface coating by α -Al₂O₃ films (Fig. 1 left). Commercial available WC-Co cemented carbides are generally coated with α -Al₂O₃ films prepared by thermal CVD (chemical vapor deposition) to enhance the hardness and to protect from heating. The deposition temperature of α -Al₂O₃ by conventional thermal CVD has been commonly more than 1300 K which is too high for Ti (C, N) -Ni due to significant diffusion of Ni into the coating layer, and its deposition rate is too low around less than several $\mu\text{m}/\text{h}$. The thick coating layer of α -Al₂O₃ more than several 10s μm is also required due to recent severe cutting conditions. Therefore, the low temperature and high-speed deposition of α -Al₂O₃ films is highly demanded to develop high performance Ti (C, N) -Ni cermet cutting tools particularly for the reduction of W usage (Fig. 1 right).

We have developed new coating techniques of novel ceramic materials with controlling nano- and macro-texture enabling low temperature and high-speed deposition, using high-power Nd:YAG [1, 2] and laser diode in a continuous mode significantly accelerating chemical reactions forming plasma around a substrate zone. We have already reported tremendously high deposition rates of YSZ (yttria stabilized zirconia), TiO₂, Y₂O₃ etc. around several 10 to a few mm/h.

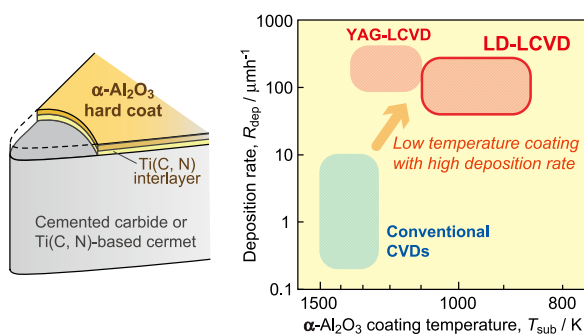


Fig. 1 Schematic of a cutting tool with α -Al₂O₃ hard coating (left) and laser CVD α -Al₂O₃ coating process by using Nd:YAG laser and laser diode (LD) (right).

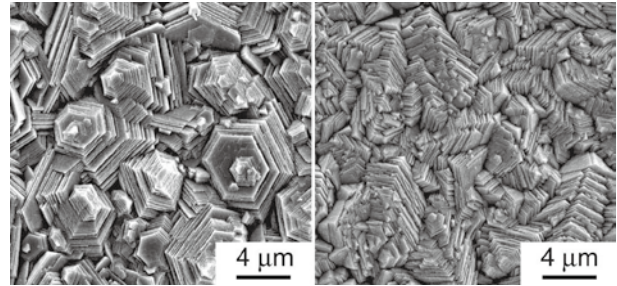


Fig. 2 Microstructure of α -Al₂O₃ coatings with (006) (left) and (104) orientation (right).

We have been taking a part of national project of “Rare Metal Substitute Materials Development Project” by the New Energy and Industrial Technology Development Organization (NEDO) since 2007, and have revealed that laser CVD (LCVD) using Nd:YAG laser is able to lower the deposition temperature about 200 K compared with conventional thermal CVD [3]. Significantly oriented and columnar textured grains have been grown with high deposition rates of 1 mm/h at most. (006) and (104) oriented α -Al₂O₃ coatings are successfully synthesized as demonstrated in Fig. 2. LCVD using diode laser is further effective to lower the deposition temperature more than 400 K less than conventional thermal CVD with significant (006) orientation which is highly required for practical coating for cutting tools due to much higher and smoother surface.

References

- [1] T. Goto, Surf. Coat. Technol. **198**, 367 (2005).
- [2] T. Goto, R. Banal, T. Kimura, Surf. Coat. Technol. **201**, 5776 (2007).
- [3] T. Goto, H. Kadokura and T. Kimura, Proceeding of 14th International Metallurgy & Materials Congress, 921 (2008).

Key Words

Laser CVD, α -alumina Coating, Rare Metal Substitute Materials

Contact to

Takashi Goto (Multi-Functional Materials Science Division)
e-mail: goto@imr.tohoku.ac.jp

Optimization of Hot Working Process by “Processing Maps”

We propose the optimization of hot working by processing map, which is demonstrated by the efficiency of power dissipation and the plastic instability parameter. In this work, friction and adiabatic corrections are conducted on the basis of experimental and theoretical considerations, and the Processing map of biomedical Co-29Cr-5Mo-0.16N alloy is established.

Hot working processes are extensively used in manufacturing products and for improving the mechanical properties of materials, etc. A fundamental method for investigating the working behavior of materials is by analyzing the true stress–true strain curves and by observing the microstructure of materials; this helps in understanding the intrinsic mechanical characteristics of materials, thereby optimizing the forging process. However, friction and temperature rise of specimen along with other factors have to be considered before further investigation [1, 2].

Processing maps, including both power dissipation and instability maps, are developed on the basis of the Dynamic Material Model. This model considers that the workpiece is a power dissipater and that the instant power dissipated at a given strain rate consists of two complementary parts: the G content and the J co-content, which are related to temperature rise and the microstructure dissipation, respectively. The factor that partitions the power between J and G is the strain-rate sensitivity (m) of the flow stress (σ); the J co-content is given by $J = \int_0^{\sigma} \dot{\epsilon} \cdot d\sigma \rightarrow \frac{\sigma \cdot \dot{\epsilon} \cdot m}{m+1}$, where $\dot{\epsilon}$ is the strain rate. The

condition for an ideal linear dissipater is $J_{\max} = \frac{\sigma \cdot \dot{\epsilon}}{2}$. For a

non-linear dissipater, the efficiency of power dissipation may be expressed in terms of a dimensionless parameter $\eta = 2m/(m+1)$. The variation of η with the temperature and strain rate constitutes the power dissipation map, and its domains may be interpreted in terms of specific microstructure processes. The occurrence of instability has been proposed by Ziegler, and a condition for microstructure-related flow instabilities is

obtained as $\xi(\dot{\epsilon}) = \frac{\partial \log(m/m+1)}{\partial \log \dot{\epsilon}} + m < 0$. The data obtained

after the friction and adiabatic corrections are used in developing the processing maps-power dissipation map and instability map. Thus, it is possible to obtain the optimum condition of the forging process without resorting to expensive and time-consuming trial-and-error methods.

The data used for constructing the power dissipation maps have to be compensated in terms of friction and adiabatic heating [1, 2]. After compensation for Co-29Cr-5Mo-0.16N alloy as a candidate of biomedical application, the instability maps, as obtained are shown in Fig. 1-3, respectively, for a strain of 0.6 [3]. The optimum condition in the power dissipation map is closely related to the Stacking Fault Energy of the materials, and in case of Co-29Cr-5Mo-0.16N alloy, the power efficiency in the range of 20-30% is best. By combing the results from both the power efficiency map and the instability map (stable regime), the best condition for hot working process can be obtained.

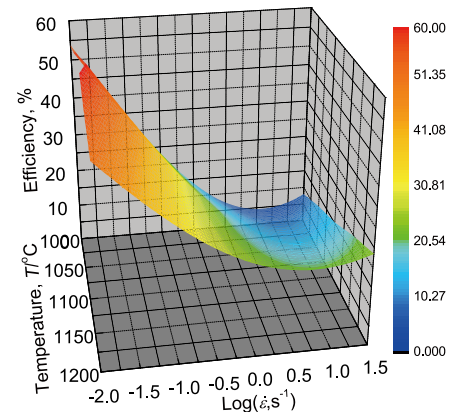


Fig. 1 3-D power dissipation map of Co-29Cr-5Mo-0.16N alloy at strain of 0.6.

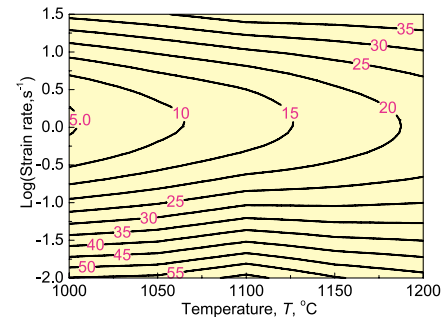


Fig. 2 Contour map of power dissipation map of Co-29Cr-5Mo-0.16N alloy at strain of 0.6.

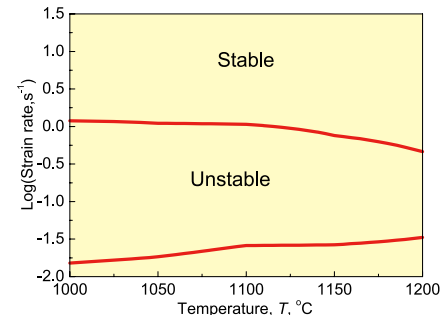


Fig. 3 Instability map of Co-29Cr-5Mo-0.16N alloy at strain of 0.6.

References

- [1] Y P Li, E. Onodera, H. Matsumoto, A. Chiba, Metall. Mater. Trans. A, 40 (2009), 982-990
- [2] Y P Li, H. Matsumoto, A. Chiba, Metall. Mater. Trans. A, 40 (2009), 2009 (40), 1203-1209.
- [3] A. Chiba, H. Lee, H. Matsumoto, M. Nakamura, Mater. Sci. Eng. A513–514 (2009) 286–293.

Key Words

Processing Map, Co-Cr-Mo Alloy, Dynamic Recrystallization

Contact to

Akihiko Chiba (Deformation Processing Division)
e-mail: a.chiba@imr.tohoku.ac.jp

X-ray Analytical Approach: Change in Dislocation Density and Precipitate Size for Copper Alloy during Aging Treatment

The correlation between growth process of precipitates and the dislocation density in a Cu-Ni-Si alloy during aging was investigated by small angle scattering (SAXS) and X-ray diffraction (XRD) methods. These X-ray analyses revealed that the rearrangement of the dislocation density in a copper matrix induced coarsening of the precipitates.

A Cu-Ni-Si system is known as one of copper alloys for industrial applications, because it exhibits high electrical conductivity as well as high strength by highly dispersed nickel-silicide precipitates formed during aging. It is well known that the precipitate coarsening, which occurs at a prolonged aging time, results in deteriorating the mechanical properties. The SAXS method can be a powerful tool for a quantitative characterization of the growth behavior of nano-precipitates in copper alloys [1, 2]. Our study using the SAXS method has suggested that a cold-rolling treatment prior to the aging treatment can stimulate coarsening of the precipitates [1]. This result indicates a high dislocation density induced by the cold-rolling treatment could have effects on the growth behavior of the precipitates. In order to validate this correlation between the growth behavior of precipitates and the dislocation of the copper matrix, the dislocation density must be estimated accurately. The characteristics on dislocation have been generally observed and discussed by an electron microscope. However, it becomes rather difficult to characterize it under the existence of highly-populated precipitates with a direct observation method. This subject prompts us to apply the XRD line-profile analysis for characterizing the dislocation. In this study, we will show several interesting behaviors of the dislocation in the copper alloy during the aging treatment.

A Cu-2.47Ni-0.58Si (wt%) alloy was prepared by a plasma arc melting method. This alloy was homogenized at 1173 K for 10^5 s, and was cut to sheets. The sheet samples were solution-treated at 1173 K for 1.8 ks, and were subsequently cold-rolled by 50 %.

Figure 1 shows the dependence of Vickers hardness of the alloy on the aging time at 720 K. The peak hardness of about 220 Hv was obtained at the aging time between 5 ks and 10 ks, and the hardness eventually dropped at the aging time of more than 20 ks.

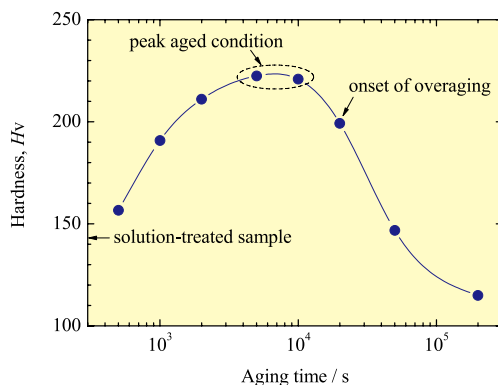


Fig. 1 The dependence of the Vickers hardness of Cu-2.47Ni-0.58Si (wt%) alloy on the aging time at 720 K. The maximum hardness appears at the aging time between 5 ks and 10 ks. The over-aged state begins at the aging time of 20 ks.

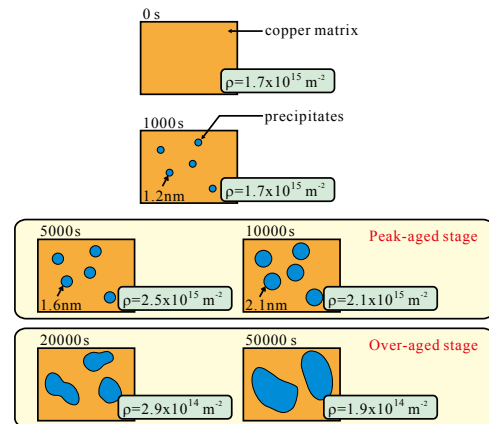


Fig. 2 Schematic diagram of the growth behavior of precipitates. The dislocation density (ρ) of the copper matrix is also denoted. The coarsening of precipitates occurred with a decrease in the dislocation density.

The SAXS measurements were carried out using a three-pin-hole camera with a two-dimensional position sensitive proportional counter. The size distribution of precipitates was estimated from the SAXS profiles using an indirect Fourier transform procedure. The schematic diagram of the growth behavior of the precipitates is illustrated in Fig. 2. As expected from Fig. 1, the precipitates grew homogeneously till the aging time of 10 ks, and then inhomogeneous precipitates having larger size were formed after the aging time of 20 ks.

The XRD profiles from the copper matrix were measured to estimate the dislocation density of the copper matrix. The diffraction profiles, which depend on the dislocation density and crystallite size of the copper matrix, varied with an increase in the aging time. The dislocation density (ρ) was estimated through the XRD line-profile analysis of the modified Williamson-Hall and modified Warren-Averbach methods [3] (Fig. 2). It is quite interesting that the dislocation density varied with the aging time in accordance with the variation of the growth behavior of precipitates. That is, the dislocation density changed only a little till the peak-aged condition (10 ks) and dropped by one order at the start of the over-aged condition (20 ks). This dependence of the dislocation density on the aging time clearly supports the mechanism we suggested [1] that the coarsening of precipitates is induced by the rearrangement of the dislocation in the copper matrix.

References

- [1] Y. Takahashi, T. Sanada, S. Sato, T. Okajima, K. Shinoda and S. Suzuki, *Mater. Trans.* **48**, 101 (2007).
- [2] S. Sato, *J. Spectrosc. Soc. Japan* **57**, 294 (2008).
- [3] T. Ungar and G. Tichy, *Phys. Stat. Sol. (a)* **171**, 425 (1999).

Key Words

Small Angle X-ray Scattering, X-ray Diffraction Line-profile Analysis

Contact to

Shigeo Sato (Analytical Science Division)
e-mail: s.sato@imr.tohoku.ac.jp

Atomic Structure Imaging of Nanoparticles by Aberration Corrected HRTEM & Exit-Wave Reconstruction

The atomic structure of FePd nanoparticles has been studied by aberration corrected high-resolution transmission electron microscopy. Chemical order is clearly seen as bright contrast, free of imaging artifacts, due to the small negative value of corrected third-order spherical aberration. The reconstructed phase image directly shows the projected potential distribution within the specimen and reveals the elemental differences due to chemical order.

Recent development of ultra-high density magnetic storage technology requires novel recording media with a higher magnetocrystalline anisotropy energy (MAE), aiming to increase the storage density and to decrease the recording noise. One of the candidates for future storage media is FePd nanoparticle with the L1₀-type ordered structure. The hard magnetic properties of this alloy nanoparticle originate from the tetragonal ordered structure with a high MAE. Therefore the atomic ordering is a key issue of hard magnetic properties. We used aberration corrected (AC) high-resolution transmission electron microscopy (HRTEM) for the imaging of chemical order [1]. Besides highly improved spatial resolution, AC-HRTEM benefits from smaller defocus values at the optimal defocus condition, almost corresponds to the Gaussian focus, due to small aberration values. This technique has now become practically available.

The FePd alloy nanoparticles studied were formed as epitaxial islands on a NaCl (001) substrate using sequential deposition of Pd and Fe followed by postdeposition annealing. HRTEM images were obtained by using an FEI Titan 80-300 TEM operating at 300 kV equipped with a field emission gun (FEG) and a CEOS image corrector [installed at Tohoku University].

Figure 1 (a) shows HRTEM image of a 10-nm-sized FePd nanoparticle with the c-axis of the L1₀ structure oriented normal to the film plane, taken at C_s = -0.34 μm (C_s: 3rd-order spherical aberration). The arrangement of atoms due to chemical order can be seen unambiguously as periodic bright contrast in the HRTEM image even at the interface between the crystal and amorphous, as well as the inside of the nanoparticle. Under the present experimental condition and with the weak phase object approximation, the projected potential is imaged as a bright contrast. Figure 1 (b) shows an HRTEM image of an ordered FePd nanoparticle with its c-axis oriented parallel to the film plane. Apparent in Fig. 1 (b)

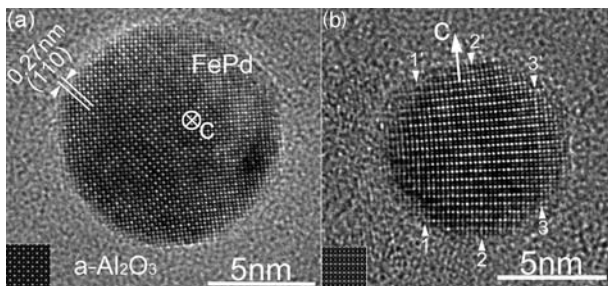


Fig. 1 (a) HRTEM image of an L1₀-FePd nanoparticle with the c-axis oriented normal to the film plane. The defocus is estimated to be -13 nm by analyzing the power spectra. (b) HRTEM image with the beam incidence of [100]_{FePd}.

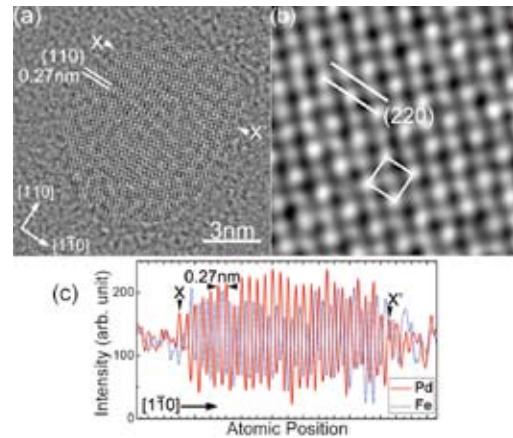


Fig. 2 (a) Phase image of exit-wave reconstructed by focal-series HRTEM images, and (b) a magnified phase image. The focal step analyzed a posteriori was 2 nm on average. The square indicates the unit cell of the ordered structure. (c) Intensity profiles for Pd and Fe rows measured in the [1 $\bar{1}$ 0] direction on the phase image.

is bending of the lattice image along the c-axis. For example, average (001) plane distance on lines 1-1' and 2-2' is distorted by -9.2% and -5.2%, respectively, relative to those on the line 3-3'. The observed distortion may have its origin in a possible compositional variation or strain distribution, however, the detail still remains an open question.

Figure 2 shows the phase of the exit-wave function by reconstructing a focal-series of HRTEM images. Two kinds of bright dots, strong and weak, arise from the potentials of Pd and Fe atoms. Figure 2 (c) shows an example of intensity profile of the reconstructed phase both for Fe and Pd. Thus, the reconstruction of phase image makes us possible to reveal the elemental difference as well as the clear-cut images of atomic rows, which can be compared to the AC HAADF-STEM images [2].

In summary, we demonstrated that the atomic structure of the L1₀-FePd nanoparticles can be observed unambiguously by AC-HRTEM. The reconstructed phase image directly shows the projected potential distribution within the specimen. The clear-cut long-range order is lost when the size of particles is smaller than about 5 nm, and locally ordered particles become dominant, indicating the instability of the ordered FePd phase. It is therefore suggested that such a size effect is likely to place limits on industrial applications of small FePd nanoparticles.

References

- [1] K. Sato, T. J. Konno and Y. Hirotsu, J. Appl. Phys. **105**, 034308 (2009).
- [2] K. Sato, J. G. Wen and J. M. Zuo, J. Appl. Phys. **105**, 093509 (2009).

Key Words

Electron Microscopy, Nanoparticle, Exit-Wave Reconstruction

Contact to

Kazuhiro Sato (Advanced Analysis of Materials Division)
e-mail: ksato@imr.tohoku.ac.jp

Malleable Hypoeutectic Zr-Ni-Cu-Al Bulk Glassy Alloys with Tensile Plastic Elongation at Room Temperature

A new bulk glassy alloy (BGA) showing macroscopic tensile plastic elongation at room temperature has been developed in hypoeutectic Zr-Ni-Cu-Al alloys with high Poisson's ratio and low Young's modulus. Hypoeutectic $Zr_{70}Ni_{16}Cu_6Al_8$ BGA exhibits the highest Poisson's ratio of 0.39 and the lowest Young's modulus 73 GPa, a distinct tensile plastic elongation of about 1.7 % and room temperature malleability in compression without fracture. The highly ductile nature seems to originate from modifications in the medium-range atomic order in hypoeutectic region.

Figure 1 (a) shows compositional dependence of Poisson's ratio of as-cast hypoeutectic Zr-Ni-Cu-Al₁₀ glassy rods of diameter 8 mm. Near the eutectic composition of $Zr_{54}Ni_6Cu_{30}Al_{10}$ [1], the Poisson's ratio decreases monotonically with increasing Cu content alone and increases with simultaneous rise in both Zr and Ni contents. $Zr_{70}Ni_{15}Cu_5Al_{10}$ BGA exhibits the highest Poisson's ratio among hypoeutectic alloys with $\mu = 0.38$. Figure 1 (b) shows the compositional dependence of Young's modulus as well as Poisson's ratio. $Zr_{70}Ni_{15}Cu_5Al_{10}$ BGA also exhibits the lowest Young's modulus of $E = 78$ GPa. Since the compositional dependence of Young's modulus in Zr-Ni-Cu-Al BGA has a positive correlation with Al content, we modify the $Zr_{70}Ni_{15}Cu_5Al_{10}$ alloy composition by decreasing slightly the Al concentration [1]. As a result, we found the Zr-enriched hypoeutectic $Zr_{70}Ni_{16}Cu_6Al_8$ glassy alloy with the highest Poisson's ratio of 0.393 ± 0.003 and the lowest Young's modulus of 73 ± 4 GPa. Consequently, the $Zr_{70}Ni_{16}Cu_6Al_8$ BGA was used for subsequent mechanical testing.

Figure 2 (a) shows the corresponding stress-strain curve. One can see a distinct linear elastic region, followed by clear yielding and then plastic elongation. Figure 2 (b-e) shows an over view of the tensile fracture surface of the $Zr_{70}Ni_{16}Cu_6Al_8$ BGA with a tensile true plastic strain of 1.7 %. Many shear band steps are observed on the surface near the wide sliding region (Fig. 2 (b)). Near the center of fracture surface, we can see the typical flower like vein patterns even in the tensile stress mode, as shown in Fig. 2 (c). Behind the fracture surface, shear band traces are seen on the outer surface, as shown in Fig. 2 (d), and the magnified image reveals the existence of many shear band steps near the fracture surface (Fig. 2 (e)). Implying the formation of a single glassy phase.

The structures of bulk metallic glasses are characterized by the packing together of efficiently packed atom clusters (chemical and

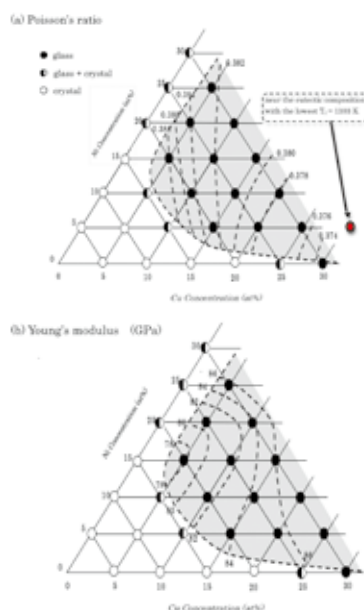


Fig. 1 Compositional dependence of Poisson's ratio (a) and Young's modulus (b) of hypoeutectic Zr-Ni-Cu-Al BGAs.

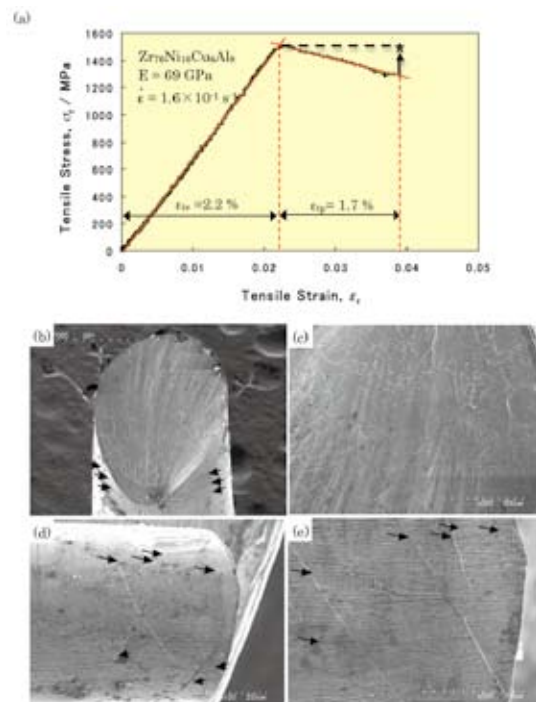


Fig. 2 Tensile true stress vs. true strain curve of hypoeutectic $Zr_{70}Ni_{16}Cu_6Al_8$ BGA (a) and SEM image of all over tensile fractured surface (b), center region of tensile fractured surface (c), behind the tensile fractured surface (d) and magnified image of region A in (d) (e). Arrow marks point out the surface steps of shear bands near the tensile fractured surface.

topological short range order (SRO) on a scale of about 0.5 nm) with the inter-cluster connectivity defining the medium range order (MRO) detectable to 1-2 nm in range by diffraction methods [2, 3]. This MRO is the same scale as the dimension of shear transformation zones (STZs), which must be stress-activated and is connected to initiate a shear band [4]. Furthermore, positron annihilation analysis of coincidence Doppler broadening experiments [5] on ternary eutectic $Zr_{50}Cu_{40}Al_{10}$ BGA reveals that free volume is surrounded by a higher fraction of Zr atoms as compared to the nominal alloy composition. The significant decrease in Young's modulus in Zr-enriched BGAs (Fig.1 (b)) may be caused by the formation of bifurcated percolation path composed of weakly bonded regions enriched in nearest Zr-Zr atom pairs.

References

- [1] Y. Yokoyama and A. Inoue, Mater. Trans. 48, 1282-1286 (2007).
- [2] Miracle, D. B., A structural model for metallic glasses, Nature Mater. 3, 697-702 (2004).
- [3] Sheng, H. W., Luo, W. K., Alamgir, F. M., Bai, J. M. & Ma, E., Atomic packing and short-to-medium-range order in metallic glasses, Nature 439, 419-425 (2006).
- [4] Yavari, A.R., A new order for metallic glasses, Nature 439, 405-406 (2006).
- [5] T. Yano, Y. Yorikado, Y. Akeno, F. Hori, Y. Yokoyama, A. Iwase, A. Inoue and T.J. Konno, Mater. Trans. 46, 2886-2893 (2005).

Key Words

Bulk Metallic Glass, Tensile Ductility, Hypoeutectic

Contact to

Yoshihiko Yokoyama (Advanced Research Center of Metallic Glasses)
e-mail: yy@imr.tohoku.ac.jp

Effect of Excess Electrons on hcp Mg and the Model Clusters for Bulk Metallic Glasses

We report the effect of excess electrons on hexagonal close-packed Mg and the model clusters explained by an inflation process using density functional theory-based calculations, in order to understand the role of conduction electron concentration in Mg-based bulk metallic glasses. We find the volume expansion and distortion to a higher c/a ratio in the negative charge state.

The role of conduction electron concentration is one of the key roles in revealing the formation mechanism of bulk metallic glasses (BMGs). The conduction electron concentration of Mg has recently been estimated to be larger in Mg-based BMGs than in crystalline magnesium. The hcp metals have a wide range in their c/a ratio from the lowest value of 1.568 for Be to the largest value of 1.886 for Cd, and the c/a ratio of 1.624 of hcp Mg corresponds virtually to the case of an ideal close packing where $c/a = \sqrt{8/3}$ (1.633). The structural diversity is reflected in their physical properties such as the melting points, cohesive energies and magnetic susceptibilities. Lowering the melting point is an issue in the formation technique of BMG. In the sense, the effect of excess electrons on the structure of hcp Mg is worthy of investigation. We have investigated the effects of excess electrons on hcp Mg and the model clusters explained by an inflation process [1]. Our aim is to understand the formation mechanism of Mg-based BMGs.

Mg-based BMGs have been formed in very wide composition ranges: $Mg_{65}Ni_{20}Nd_{15}$, $Mg_{70}M1_xM2_{30-x}$, $Mg_{75}M1_xM2_{25-x}$, $Mg_{77}Ni_{18}Nd_5$, $Mg_{80}M1_xM3_{20-x}$, $Mg_{85}Cu_5Y_{10}$ for $M1 = Ni, Cu$, $M2 = Nd, Y$ and $M3 = Nd, Sn, Y$, where Mg-rich BMGs are excluded. The ratios of magnesium to $3n$ additives ($n = 0, 1, 2, \dots$) are 17 : 9, 7 : 3, 3 : 1, 10 : 3, 4 : 1, and 17 : 3, respectively. From the ratios, we consider Mg_3 , Mg_4 , Mg_7 , Mg_{10} and Mg_{17} as model clusters and examine the

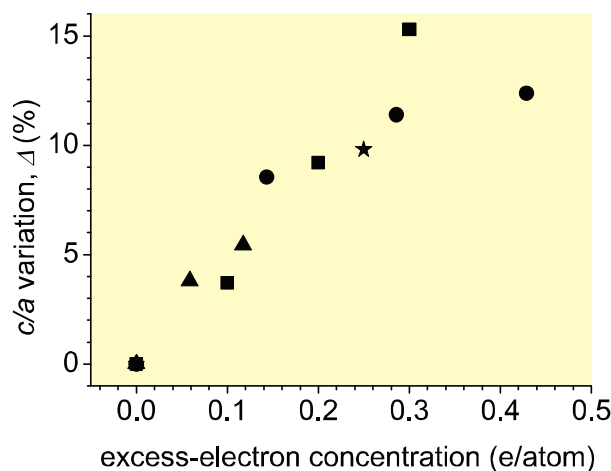


Fig. 1 Normalized c/a variation (%), Δ , vs. the excess-electron concentration (e/atom) for Mg_7 (●), Mg_{10} (■), Mg_{17} (▲), and hcp Mg (★). $\Delta = 1/N \times ((c/a \text{ of charge state}) / (c/a \text{ of neutral state}) - 1) \times 100$. For clusters, $c = L_1/N$, $a = L_2$. $N = 1, 1.5, 3$, and 0.5 for Mg_7 , Mg_{10} , Mg_{17} , and hcp Mg, respectively.

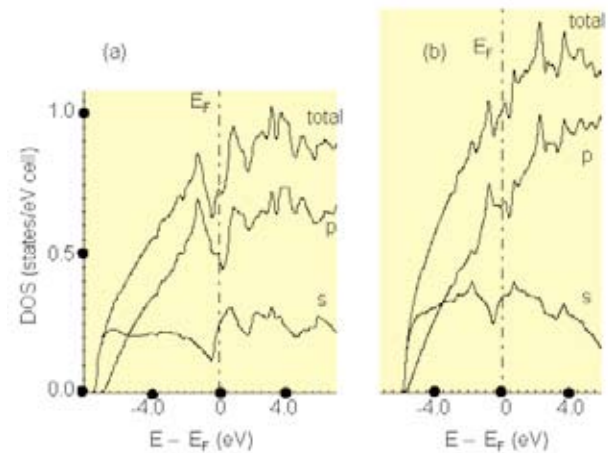


Fig. 2 Total and partial densities of states (DOS) of hcp Mg. (a) Neutral state. (b) At the expanded lattice constants by charging but with no excess electron.

effect of excess electrons. The inflation rule, $A \rightarrow AB$ and $B \rightarrow A$ where $A = Mg_3$, $B = Mg_4$, leads to the consecutive sequences, $S_0 = A$ (Mg_3), $S_1 = AB$ (Mg_7), $S_2 = ABA$ (Mg_{10}) and $S_3 = ABAAB$ (Mg_{17}).

Both in the clusters (Mg_7 , Mg_{10} and Mg_{17}) and hcp Mg, the c/a ratio increases proportionally to the concentration of excess electrons (Fig. 1) and the cell volume expands. The charged clusters up to dianion are more stable than the corresponding neutral clusters, suggesting that the increase in the conduction electron concentration of Mg in BMGs is possible to stabilize the cluster structures. The distortion to a higher c/a ratio suggests that the melting point would be lowered in the charge state. The pseudogap by s - p mixing at the Fermi level is weakened in the expanded cell with a distorted c/a ratio and a new spiky structure mainly contributed by p bands appears (Fig. 2), indicating a signature of states preferentially localized around the structural cluster which occurs in quasicrystalline materials. It would be anticipated that the expanded volume and the distorted c/a ratio by the charge transfer from additives suppress the crystallization of supercooled liquid. Further theoretical study on Mg-Cu-Y systems is required.

References

[1] M. Takahashi, M. Fukuhara, A. Inoue, Y. Kawazoe, J. Phys. D: Appl. Phys **41**, 155424 (2008).

Key Words

Bulk Metallic Glass, Magnesium Clusters, Density Functional Theory Calculations

Contact to

Masae Takahashi (Advanced Research Center of Metallic Glasses)

e-mail: masae@imr.tohoku.ac.jp

Development of Iron-group Based Glassy Alloy with High Deformability and High Folding Endurance

Fe-, Ni- and Co-based glassy alloys have been developed with modifying to meet the needs for application. Since folding endurance value of the developed Ni-based glassy alloy is 10 times as large as that of stainless SUS304 steel, it become possible to develop highly flexible precision products.

Fe-, Ni- and Co-based (Iron-group based) amorphous alloys are marketed in ribbon or wire form, and are used in various fields. To produce the precision and small parts with Iron-group based amorphous alloy in ribbon or wire form, the improvement of the alloy is expected in imprintability and folding endurance.

High plastic deformability with Newtonian viscous flow of the amorphous alloy (glassy alloy) allows imprinting of a precision component. Figure 1 (a) and (b) show the SEM images of the surface morphology of the electroformed Ni die and the imprinted (Fe_{0.73}Ga_{0.04}P_{0.11}Co_{0.05}B_{0.04}Si_{0.03})₉₉Cr₁ glassy alloy ribbon [1]. The surface structure of the imprinted sample exhibits the wave shape with 1 μm period, and that is similar to the shape of the original Ni die. The super-cooled liquid region defined by temperature interval between the glass transition temperature and crystallization temperature is 45 K for (Fe_{0.73}Ga_{0.04}P_{0.11}Co_{0.05}B_{0.04}Si_{0.03})₉₉Cr₁ glassy alloy. The Iron-group based glassy alloy with large super-cooled liquid region allows imprinting. To raise the imprintability of glassy alloy, it is important to expand the super-cooled liquid region of the alloy. Figure 2 shows the DSC curves of Co₄₈Cr₁₅Mo₁₄Tm₂C₁₅B₆ and Ni₆₅Cr₁₅Si₇B₁₃ glassy alloy samples [2, 3]. It can be seen an endothermic reaction due to glass transition, followed by a super-cooled liquid region and then an exothermic reaction due to crystallization. The CoCrMoCBTm and NiSiBCr glassy alloy exhibit large super-cooled liquid region of 90 K and 63 K, respectively. These Iron-group based glassy alloys are suitable for imprint processing in the super-cooled liquid region to fabricate the small precision parts.

The small parts with glassy alloy are flexible and bend easily, but the annealed parts with imprinting or coating may lose those properties. The annealed glassy alloys need to have good flexible durability. The flexible durability of the products with metal and/or polymer film is evaluated by the MIT folding endurance test. Figure 3 shows the results of the MIT folding endurance test of the ribbons with a thickness of 0.03 mm. The MIT folding endurance value is defined as the number of times a ribbon can be bended without breaking on the MIT folding endurance tester. Although the MIT folding endurance value of the FeSiB amorphous alloy decreases significantly with annealing because of embrittlement of the amorphous phase, the values of Ni-based alloy exhibit little change with annealing.

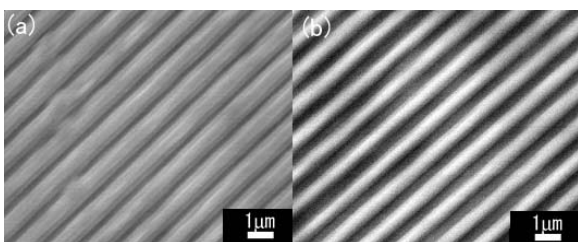


Fig. 1 The SEM images of the surface morphology of (a) Ni die and (b) the imprinted (Fe_{0.73}Ga_{0.04}P_{0.11}Co_{0.05}B_{0.04}Si_{0.03})₉₉Cr₁ glassy alloy ribbon

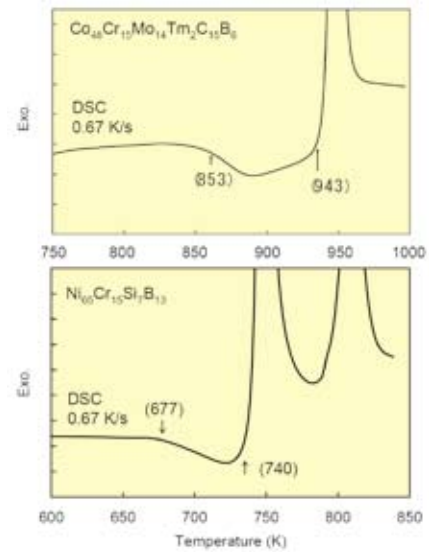


Fig. 2 The DSC curves of the Co₄₈Cr₁₅Mo₁₄Tm₂C₁₅B₆ and Ni₆₅Cr₁₅Si₇B₁₃ glassy alloy samples

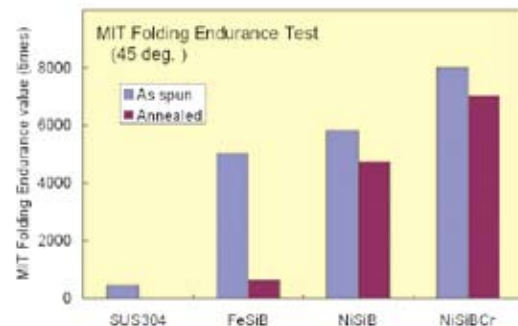


Fig. 3 The MIT folding endurance values of a Ni₇₅Si₈B₁₇ amorphous alloy and Ni₆₅Cr₁₅Si₁₀B₁₀ glassy alloy, and those of a FeSiB amorphous alloy and stainless SUS304 steel are shown for comparison

The value of the annealed Ni₆₅Cr₁₅Si₁₀B₁₀ glassy alloy with super-cooled liquid region is 10 times as high as that of stainless steel [3]. These results suggest that the NiCrSiB glassy alloy is an imprintable and flexible material. Furthermore, the alloy exhibits high corrosion resistance. These glassy alloys are promising imprintable materials with high performance.

References

- [1] K. Amiya, Y. Saotome, N. Nishiyama, A. Urata, A. Inoue: Proc. Asian Workshop Nano/micro Forming Tech. (2007).
- [2] K. Amiya and A. Inoue, Rev. Adv. Mater. Sci., **18**, 27(2008).
- [3] Pat.Pend, JP-A(2008)

Key Words

Glassy Alloy, Imprint, Folding Endurance

Contact to

Kenji Amiya (Osaka Center for Industrial Materials Research)
e-mail: amiya.k@imr.tohoku.ac.jp

Discovery of Spin-Motive Force — “Spin Battery” Using Nano-Magnets —

The existence of a spin-motive force, a correction to Faraday’s law of induction, has been proven in experiment using a magnetic tunnel junction with nano-meter-sized magnetic particles [1]. This discovery enables direct conversion between magnetic and electrical energies, which opens the way for applications in ultra-high sensitivity magnetic sensors as well as new type of “spin batteries.”

Electrical currents usually correspond to a flow of electrons, elementary particles that carry a tiny electrical charge, $-e$. In 1930, Dirac showed that, in order to be consistent with Einstein’s special relativity and quantum mechanics, an electron must also have “spin,” in effect, being a tiny magnet (Fig.1). “Spintronics” is an emerging electronics technology in which the electron spin is used in an essential manner [2]. The issues studied in this field include tunneling magnetoresistance, domain wall motion due to magnetic fields or electric currents in ferromagnets.

One of the versatile methods to generate electric power for driving various electronic devices is Faraday’s law of induction, a fundamental principle dating from 1831. The usual Faraday’s law determines an electromotive force (e.m.f.) ε as

$$\varepsilon = -d\Phi/dt,$$

where Φ is the magnetic flux. To derive this law, only forces resulting from the charge of electrons have been accounted for. In ferromagnetic materials, however, there exist nonconservative “spin forces” which also contribute to the e.m.f. [3]. These might be included in Faraday’s law if Φ is replaced by $[\hbar/(-e)]\gamma$,

$$\varepsilon = -[\hbar/(-e)]d\gamma/dt,$$

where $\gamma = \gamma_e + \gamma_s$ is a “Berry phase.” $\gamma_e = [(-e)/\hbar]\Phi$ recovers the usual charge part of Faraday’s law while γ_s represents the spin contribution suitably averaged over the electron spin direction. The latter contribution to ε refers time dependent magnetization in general. One of the remarkable implications is the fact that the e.m.f. can be induced even by a ‘static’ magnetic field when that field drives magnetization dynamics. The anticipated effect, however, remained elusive until recently.

The research group consisted of Professor S. Maekawa (Institute for Materials Research, Tohoku University), Professor M. Tanaka (Department of Electrical Engineering and Information Systems, The University of Tokyo), and Professor S. E. Barnes (Physics Department, University of Miami) found that such an e.m.f can indeed be induced by a static magnetic field in magnetic tunnel junctions containing zinc blende-structured MnAs quantum nanomagnets (Fig. 2). The observed e.m.f results from the conversion of the magnetic energy of the super-paramagnetic MnAs nanomagnets into electrical energy when these magnets undergo magnetic quantum tunneling. Due to the quantum nature of the nanomagnets, the produced e.m.f. is over a hundred times larger and for tens of minutes, rather than for

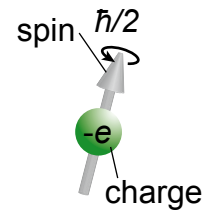


Fig. 1 An electron has charge and spin degrees of freedom.

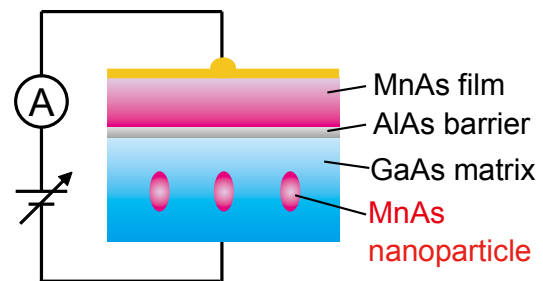


Fig. 2 A schematic illustration of the device structure.

milliseconds as expected. As a consequence, a huge magnetoresistance of up to 100,000 per cent is observed for certain bias voltage. Their results strongly supported the contention that, in magnetic nanostructures, Faraday’s law of induction must be generalized to account for forces of purely spin origin. The huge magnetoresistance and e.m.f. may find potential applications in high sensitivity magnetic sensors, as well as in new active devices such as “spin batteries.”

References

- [1] P. N. Hai, S. Ohya, M. Tanaka, S. E. Barnes & S. Maekawa, *Nature* **458**, 489 (2009).
- [2] S. Maekawa ed., *Concepts in Spin Electronics* (Oxford University Press, Oxford, 2006).
- [3] S. E. Barnes and S. Maekawa, *Phys. Rev. Lett.* **98**, 246601 (2007).

Key Words

Spintronics, Spin-motive Force, Huge Magnetoresistance

Contact to

Sadamichi Maekawa (Materials Property Division)
e-mail: Maekawa@imr.tohoku.ac.jp